

No Sun-like dynamo on the active star ζ Andromedae from starspot asymmetry

R. M. Roettenbacher¹, J. D. Monnier¹, H. Korhonen^{2,3}, A. N. Aarnio¹, F. Baron^{1,4}, X. Che¹, R. O. Harmon⁵, Zs. Kővári⁶, S. Kraus^{1,7}, G. H. Schaefer⁸, G. Torres⁹, M. Zhao^{1,10}, T. A. ten Brummelaar⁸, J. Sturmann⁸, & L. Sturmann⁸

¹Department of Astronomy, University of Michigan, Ann Arbor, MI 48109, USA

²Finnish Centre for Astronomy with ESO (FINCA), University of Turku, FI-21500 Piikkiö, Finland

³Dark Cosmology Centre, Niels Bohr Institute, University of Copenhagen, Juliane Maries Vej 30, DK-2100 Copenhagen Ø, Denmark

⁴Department of Physics and Astronomy, Georgia State University, Atlanta, GA 30303 USA

⁵Department of Physics and Astronomy, Ohio Wesleyan University, Delaware, OH 48103 USA

⁶Konkoly Observatory, Research Center for Astronomy and Earth Sciences, Hungarian Academy of the Sciences, H-1121 Budapest, Konkoly Thege Miklós út 15-17, Hungary

⁷School of Physics, University of Exeter, Exeter, EX4 4QL, UK

⁸Center for High Angular Resolution Astronomy, Georgia State University, Mount Wilson, CA 91023, USA

⁹Harvard-Smithsonian Center for Astrophysics, 60 Garden Street, Cambridge, MA 02138, USA

¹⁰Department of Astronomy & Astrophysics, Pennsylvania State University, State College, PA 16802, USA

Sunspots are cool areas caused by strong surface magnetic fields inhibiting convection^{1,2}. Moreover, strong magnetic fields can alter the average atmospheric

structure³, degrading our ability to measure stellar masses and ages. Stars more active than the Sun have more and stronger dark spots than in the solar case, including on the rotational pole itself⁴. Doppler imaging, which has so far produced the most detailed images of surface structures on other stars than the Sun, cannot always distinguish the hemisphere in which the starspots are located, especially in the equatorial region and if the data quality is not optimal⁵. This leads to problems in investigating the north-south distribution of starspot active latitudes (those latitudes with more spot activity), which are crucial constraints of dynamo theory. Polar spots, inferred only from Doppler tomography, could plausibly be observational artifacts, casting some doubt on their very existence⁶. Here we report imaging of the old, magnetically-active star ζ Andromedae using long-baseline infrared interferometry. In our data, a dark polar spot is seen in each of two epochs, while lower-latitude spot structures in both hemispheres do not persist between observations revealing global starspot asymmetries. The north-south symmetry of active latitudes observed on the Sun⁷ is absent on ζ And, which hosts global spot patterns that cannot be produced by solar-type dynamos⁸.

ζ And is a nearby active star that is both spatially large and spotted, making it one of a small number of promising imaging targets with current interferometric capabilities. ζ And is a tidally-locked close binary (RS CVn) system consisting of a K-type cool giant and an unseen lower-mass companion star⁹. Tidal interactions have spun-up the cool primary component, causing unusually strong starspots and magnetic activity^{4,10}.

We observed ζ And during two observing campaigns of eleven nights spanning UT 2011 Jul 9-22 and fourteen nights spanning UT 2013 September 12-30 (see Extended Data Table 1)

with the Michigan InfraRed Combiner (MIRC)¹¹ using all six telescopes at Georgia State University's Center for High Angular Resolution Astronomy (CHARA) Array¹² on Mount Wilson, CA, USA.

The 2011 and 2013 datasets were separately imaged onto a prolate ellipsoid via the imaging software SURFING (SURFace ImagING), an aperture synthesis imaging technique (Monnier, in preparation). This novel approach replicates the fundamental ideas behind Doppler imaging in that the whole data set is mapped onto the rotating surface at once instead of night-by-night snapshots. Treating each dataset as an ensemble also allows SURFING to fit stellar and orbital parameters (see Table 1) along with the surface temperature maps (see Figures 1 and 2).

The surface temperature maps for ζ And show peaks of 4530 K and 4550 K and minimum values of 3540 K and 3660 K in 2011 and 2013, respectively. The ~ 900 K range of temperatures we see across the surface is slightly larger than the ~ 700 K found from recent Doppler imaging work (from the Fe I 6430 Å line). A strong dark polar spot is present in both of our imaging epochs, also consistent with recent Doppler imaging studies^{7,13,14}. In contrast to this persistent feature, many other large dark regions completely change from 2011 to 2013 with no apparent overall symmetry or pattern. These features and their locations are only unambiguously imaged by interferometry, since Doppler and light-curve inversion imaging techniques experience latitude degeneracies (see Methods section for more details). We now discuss the starspot implications on the dynamical large-scale magnetic field of ζ And.

The extended network of cool regions stretching across the star suggest that strong magnetic fields can suppress convection on *global* scales, not just local concentrations forming spot structures. The extent to which starspots can cover the surface of a star is presently unknown and of interest in understanding how activity saturates on rapidly-rotating, convective

stars¹⁵. The observations in hand lend support to studies that have suggested magnetic activity can be so widespread as to alter the apparent fundamental parameters of a star^{16,17}. For example, a larger region of suppressed convection gives a lower observed temperature, leading to inaccurate estimates for stellar mass and age³. The changes in global magnetic features will produce long-term photometric variations that are often only attributed to changes in a growing or shrinking polar starspot. We note that a polar starspot for ζ And does not affect the flux of the star as significantly as other large-scale magnetic structures due to the effects of limb darkening and foreshortening on this highly inclined system ($i \sim 70.0^\circ$).

The interferometric images of ζ And provide a clear confirmation of the existence of polar spots. Polar spots have been seen in Doppler images of ζ And^{9,13,14} and many other active stars⁴. Polar spots produce spectral line-profile changes only in the line core itself (no Doppler shift), and the spectral signature of a symmetric polar spot is the same at each rotational phase of the star. This signature makes polar spots very easy to be produced as artifacts in the Doppler imaging process; if the depth of the spectral line-profile is not correctly modeled, then the image will exhibit a polar spot. Strong chromospheric activity has also been postulated to fill in at least some of the photospheric lines used in Doppler imaging, potentially producing a polar spot^{18,19}. These facts made the reliability of polar spots highly debated in the early days of Doppler imaging^{20,21} and the independent confirmation of their existence here is highly significant.

The interferometric images of ζ And presented here reveal the exact hemispheres of the spots and show strong asymmetries between the hemispheres, with 2011 map showing dominant spots on the northern and the 2013 on the southern hemisphere. On the Sun the spots are typically seen on both hemispheres in certain active mid-latitude regions, with some breaking of the symmetry in the spot numbers on the two hemispheres⁷ but not as large of an asymmetry as

seen on the ζ And. Such asymmetries require a departure from the solar-type $\alpha\Omega$ -dynamo to a more complicated dynamo, such as one with mixed parity modes²².

While our results only strictly apply for giant stars in RS CVn binaries, we note strong parallels between the physical conditions and magnetic behavior of these and pre-main sequence stars. To reach these conditions, the giant primary stars in RS CVn binaries rotate rapidly due to tidal spin-up and pre-main sequence stars rotate rapidly due to contraction and angular momentum transfer due to accretion of material from a circumstellar disk. These similar physical conditions hint at shared field-generation mechanisms that are observationally indistinguishable²³ and manifest as starspots. In young associations, it has been noted that derived ages are likely strongly affected by global suppression of convection³. These commonalities and the known consequences argue that strong stellar magnetism must be accounted for in stellar models for both pre-main sequence and giant stages of evolution for the most active stars.

Results from imaging studies using light-curve inversion and Doppler imaging techniques, as well as new interferometric spot studies²⁴, all re-enforce the picture that global magnetic structures cover the faces of the most active stars. Our interferometric imaging has found unambiguous signposts of these structures and clearly points to a perspective beyond the typical isolated spots observed on the Sun. The large-scale suppression of convection by these large-scale fields will have structural effects on the stellar atmosphere, including puffing up the star and decreasing the effective temperature and luminosity, dramatic alterations that must be accounted for by modern stellar structure calculations especially for young, low-mass stars that universally show strong magnetic activity^{3,25}. In order to understand these structural effects, we must image with as much detail as possible more targets. The procedures used here can provide

similar H -band images for a handful of bright, spatially-large, spotted stars (e.g. σ Geminorum, λ Andromedae). Impending advances in visible interferometry will allow for similar resolution on more stars (down to $\theta \sim 1.1$ mas). For stars that cannot be resolved in detail, combining interferometrically-observed photocenter shifts due to rotation of starspots in and out of view with Doppler imaging would resolve degeneracies inherent in the Doppler images allowing for more accurate surface maps. By acquiring a number of these maps on several stars or a few epochs of the same targets, we would be able to understand how the changing magnetic field affects our observations of stellar parameters (including mass and age)^{3,26} and leads to new dynamo models, which will shed light on the impact of magnetism on stellar evolution^{27,28}.

1. Hale, G. E. On the Probable Existence of a Magnetic Field in Sun-Spots. *Astrophys. J.*, **28**, 315-343 (1908).
2. Biermann, L. Der gegenwärtige Stand der Theorie konvektiver Sonnenmodelle. *Vierteljahresschrift der Astronomischen Gesellschaft*, **76**, 194-200 (1941).
3. Somers, G. and Pinnsonneault, M. H. Older and cooler: the impact of starspots on pre-main-sequence stellar evolution. *Astrophys. J.*, **807**, 174 (2015).
4. Strassmeier, K. G. Starspots. *Astron. Astrophys. Rev.*, **17**, 251-308 (2009).
5. Piskunov, N. E., Tuominen, I., and Vilhu, O. Surface imaging of late-type stars. *Astron. Astrophys.*, **230**, 363-370 (1990).
6. Bruls, J. H. M. J., Solanki, S. K., and Schuessler, M. Doppler imaging: the polar SPOT controversy. *Astron. Astrophys.*, **336**, 231-241 (1998).
7. Hathaway, D. F. The Solar Cycle. *Living Rev. Solar Phys.*, **12**, 4 (2015).

8. Norton, A. A., Charbonneau, P., and Passos, D. Hemispheric Coupling: Comparing Dynamo Simulations and Observations. *Space Science Reviews*, **186**, 251-283 (2014).
9. Kóvári, Zs., et al. Doppler imaging of stellar surface structure. XXIII. The ellipsoidal K giant binary ζ Andromedae. *Astron. Astrophys.*, **463**, 1071-1080 (2007).
10. Berdyugina, S. Starspots: a key to the stellar dynamo. *Liv. Rev. in Solar Phys.*, **2**, 8 (2005).
11. Monnier, J. D., Berger, J.-P., Millan-Gabet, R., & ten Brummelaar, T. A. The Michigan Infrared Combiner (MIRC): IR imaging with the CHARA Array. *Proc. SPIE*, **5491**, 1370-1378 (2004).
12. ten Brummelaar, T. A., et al. First results from the CHARA Array. II. A description of the instrument. *Astrophys. J.*, **628**, 453-465 (2005).
13. Korhonen, H., et al. Ellipsoidal primary of the RS CVn binary ζ Andromedae. Investigation using high-resolution spectroscopy and optical interferometry. *Astron. Astrophys.*, **515**, A14 (2010).
14. Kóvári, Zs., et al. Measuring differential rotation of the K-giant ζ Andromedae. *Astron. Astrophys.*, **539**, A50 (2012).
15. Reiners, A., Basri, G., and Browning, M. Evidence for Magnetic Flux Saturation in Rapidly Rotating M Stars. *Astrophys. J.*, **692**, 538-545 (2009).
16. Spruit, H. C. Effect of spots on a star's radius and luminosity. *Astron. Astrophys.*, **108**, 348-355 (1982).
17. López-Morales, M. On the correlation between the magnetic activity levels, metallicities, and radii of low-mass stars. *Astrophys. J.*, **660**, 732-739 (2007).
18. Unruh, Y. C. and Collier Cameron, A. Does chromospheric emission mimic polar starspots in Doppler images? *Mon. Not. R. Astron. Soc.*, **290**, L37-L42 (1997).

19. Bruls, J. H. M. J., Solanki, S. K., and Schuessler, M. Doppler imaging: the polar SPOT controversy. *Astron. Astrophys.*, **336**, 231-241 (1998).
20. Strassmeier, K. G. et al. Doppler imaging of high-latitude SPOT activity on HD 26337. *Astron. Astrophys.*, **247**, 130-147 (1991).
21. Piskunov, N. and Wehlau, W. H. The detectability of cool polar caps on late type stars. *Astron. Astrophys.*, **289**, 868-870 (1994).
22. Bushby, P. J. Strong asymmetry in stellar dynamos. *Mon. Not. R. Astron. Soc.*, **338**, 655-664 (2003).
23. Bouvier, J. and Bertout, C. Spots on T Tauri stars. *Astron. Astrophys.*, **211**, 99-114 (1989).
24. Parks, J. R., et al. First images of cool starspots on a star other than the Sun: interferometric imaging of λ Andromedae. submitted to *Astrophys. J.* (2016).
25. Oláh, K., et al. Magnitude-range brightness variations of overactive K giants. *Astron. Astrophys.*, **572**, A94 (2014).
26. Stassun, K. G., Kratter, K. M., Scholz, A., & Dupuy, T. J. An empirical correction for activity effects on the temperatures, radii, and estimated masses of low-mass stars and brown dwarfs. *Astrophys. J.*, **756**, 47 (2012).
27. MacDonald, J. & Mullan, D. J. Structural effects of magnetic fields in brown dwarfs. *Astrophys. J.*, **700**, 387-394 (2009).
28. Chabrier, G., Gallardo, J., & Baraffe, I. Evolution of low-mass star and brown dwarf eclipsing binaries, *Astron. Astrophys.*, **472**, L17-L20 (2007).
29. ESA The Hipparcos and Tycho Catalogues, ESA SP-1200 (Noordwijk: ESA) (1997).
30. Fekel, F. C., Strassmeier, K. G., Weber, M., & Washuettl, A. Orbital elements and physical parameters of ten chromospherically active binary stars. *Astron. Astrophys. Sup. Ser.*, **137**, 369-383 (1999).

Full Methods and associated references are available online.

Acknowledgements

We thank E. Pedretti for his early efforts in imaging ζ And. The CHARA Array is funded through NSF grants AST-0908253 and AST 1211129 and by Georgia State University through the College of Arts and Sciences. The MIRC instrument at the CHARA Array was funded by the University of Michigan. The 2013 CHARA/MIRC observations were supported by a Rackham Graduate Student Research Grant from the University of Michigan. This imaging work was supported by the National Science Foundation (NSF) grant AST-1311698. SURFING was partially developed with funding from the Observatoire de Paris, Meudon. This research made use of the SIMBAD database, operated at CDS, Strasbourg, France and the Jean-Marie Mariotti Center SearchCal and Aspro2 services co-developed by the FIZEAU and LAOG/IPAG. This work was supported by the Hungarian Scientific Research Fund (OTKA K-109276) and “Lendület-2009” Young Researchers’ Program of the Hungarian Academy of Sciences.

Author Contributions

RMR, JDM, FB, XC, SK, and MZ obtained the observations of ζ And. RMR, JDM, FB, XC, SK, GHS, and MZ obtained the observations of 37 And. RMR performed the data reduction and calibration. RMR and GT determined the orbital parameters of 37 And. JDM and RMR created the images of ζ And, which were interpreted by RMR, JDM, HK, ZsK, ROH, and ANA. TAtB, GHS, JS, and LS provided observational setup and technical support.

Reprints and permissions information is available at www.nature.com/reprints.

Correspondence and requests for materials should be addressed to rmroett@umich.edu.

Table 1 – Parameters of ζ And.

Parameter	Value
Angular polar diameter, θ_{LD} (mas)	2.502 ± 0.008
Polar radius (R_{\odot})	15.0 ± 0.8
Oblateness (major to polar axis)	1.060 ± 0.011
Inclination, i ($^{\circ}$)	70.0 ± 2.8
Pole position angle ($^{\circ}$, E of N)	126.0 ± 1.9
Values from Literature	
Distance, d (pc)	$17.98 \pm 0.83^{[29]}$
Effective temperature, T_{eff} (K)	$4600 \pm 100^{[9]}$
Luminosity, $\log L/L_{\odot}$	$1.98 \pm 0.04^{[9]}$
Primary mass (M_{\odot})	$2.6 \pm 0.4^{[9]}$
Secondary mass (M_{\odot})	$\sim 0.75^{[9]}$
Iron metallicity $[\text{Fe}/\text{H}]/[\text{Fe}/\text{H}]_{\odot}$	$-0.30 \pm 0.05^{[9]}$

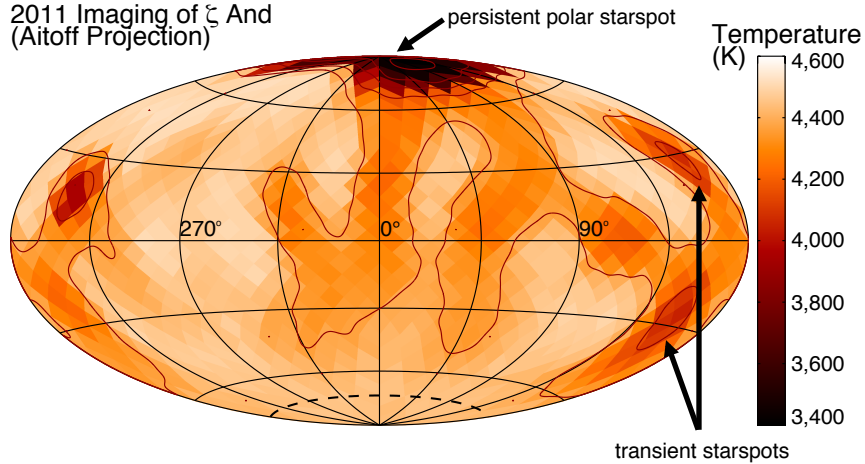
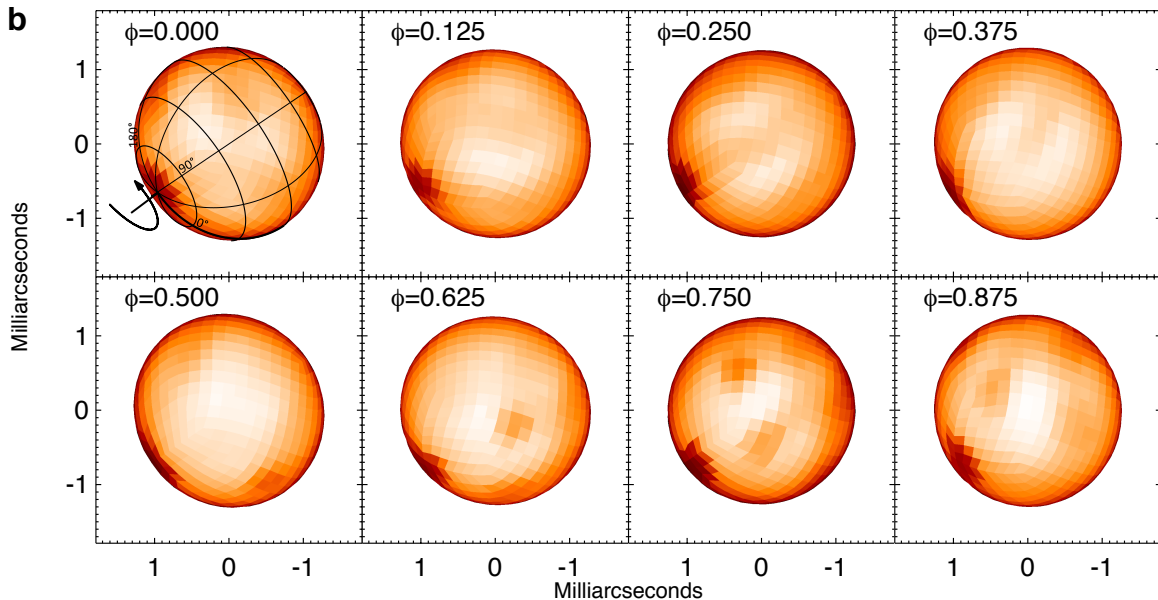
SURFING models assumed circular orbit ($e = 0$) using circular radial velocity conventions with an orbital period $P_{\text{orb}} = 17.7694260 \pm 0.00004$ days and time of nodal passage $T_0 = 49992.281 \pm 0.017$ (MJD)³⁰. Limb darkening was held fixed with power-law exponent $\mu = 0.269$, appropriate for ζ And based upon spectral type.

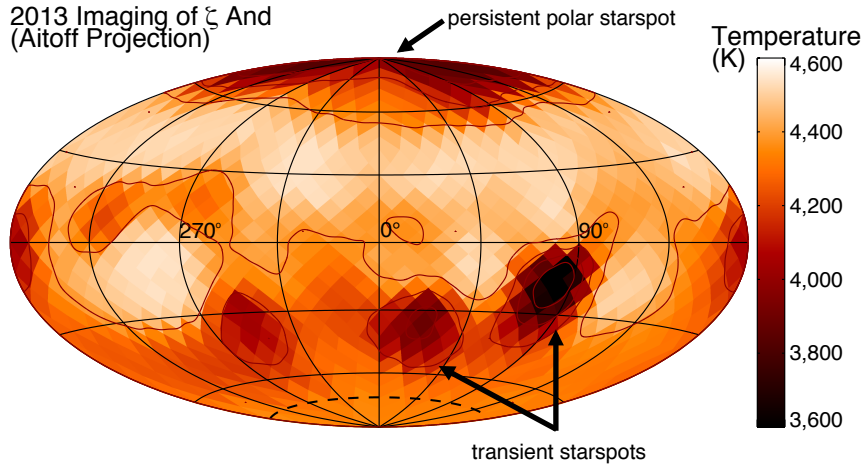
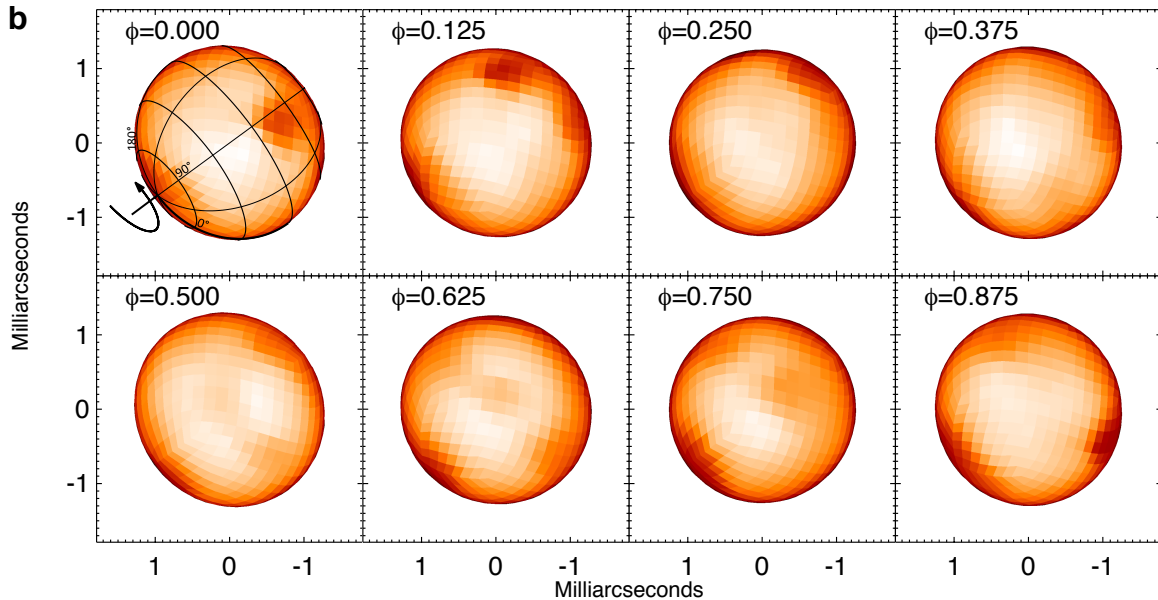
Figure 1 – Surface image of ζ And from 2011 July with eleven nights of data using

SURFING. **a**, The temperature of ζ And is presented in an Aitoff projection. The contours represent every 200 K from 3400-4600 K. The dashed line at the bottom pole is hidden due to inclination. Arrows point to example starspots. **b**, The surface reflects how the star is observed on the sky with H -band intensities (mean $H = 1.64$). The $\phi = 0.000$ plot shows longitude 0° at the bottom right of the star with 90° across the middle. The phases assume circular orbit radial velocity conventions.

Figure 2 – Surface images of ζ And from 2013 September with fourteen nights of data

using SURFING. These images are presented as in Figure 1, except the 200 K contours of the Aitoff projection (**a**) range from 3600-4600 K. The polar spot is observed to have evolved between the two sets of observations. The lower-latitudes spot present in the 2011 data set are not present in the 2013 data set, with the new spots mostly located below the equator, emphasizing the spot-latitude asymmetry observed.

a2011 Imaging of ξ And
(Aitoff Projection)**b**

a2013 Imaging of ζ And
(Aitoff Projection)**b**

Methods

Starspot Imaging Methods

Large spots covering a substantial fraction of the stellar surface have been indirectly imaged using light-curve inversion and Doppler imaging techniques^{31,32}. Light-curve inversion reproduces spotted stellar surfaces based on time-series data and can only reproduce structures observed as rotational modulations—structures such as static polar spots are practically invisible to light-curve inversion imaging. Light-curve inversion typically reveals only weak relative latitude information for the spots, although this can be improved with the combination of concurrent observations in multiple filters³³. A more detailed surface map, both in latitude and longitude, can be obtained with Doppler imaging, which creates surface temperature maps from tracking small changes in absorption lines as starspots rotate in and out of view³². Still, this method cannot always distinguish the hemisphere in which the structures are located. In order to confirm the important findings from these methods and to firmly understand global characteristics of activity that can alter stellar radii and effective temperature, a more direct imaging method is required that is immune to these ambiguities.

The nearest magnetically-active stars are too small to be resolved by even our largest telescopes. However, long-baseline interferometry has the potential to image sub-milliarcsecond features on the surfaces of nearby stars. To date, interferometric imaging has been successfully used to confirm the oblateness and gravity darkening of rapidly-rotating stars³⁴ and even to image a spotted stellar surface²⁴. To improve the resolution and imaging quality for rotating stars that show strong magnetic activity, we debut here an “imaging-on-a-sphere” technique that uses interferometric observations from multiple nights to constrain a surface temperature map.

This naturally takes advantage of the multiple views we have of starspot structures as they rotate across the disk of the star. Interferometric imaging produces unique images that resolve the degeneracies in latitude of Doppler imaging and provides the first independent confirmation of the existence of polar starspots.

Interferometric Data

Our interferometric observations were obtained using the Michigan InfraRed Combiner (MIRC) at the Center for High Angular Resolution Astronomy (CHARA) Array. The CHARA Array consists of six 1-m telescopes in a Y-shaped configuration with baselines ranging from 34 to 331 m^[12]. For the ζ And data, MIRC¹¹ combined light from all six CHARA Array telescopes in the *H*-band (eight channels across 1.5-1.8 μm for $\lambda/\Delta\lambda \sim 40$), resulting in an angular resolution of $\lambda/2B \sim 0.5$ milliarcseconds.

The data were reduced and calibrated with the standard MIRC pipeline³⁵. We searched without success for evidence of the faint companion in our interferometry data using our proven grid search method³⁶, and could only secure a 1- σ lower limit of 300:1 on the *H*-band flux ratio between primary and companion.

The data products obtained from reducing the CHARA/MIRC data with the standard pipelines consist of visibilities, closure phases, and triple amplitudes. Representative samples of the visibilities and closure phases are presented in Extended Data Figures 1 and 2 for a single night (UT 2013 September 15) of six-telescope CHARA/MIRC observations of ζ And. The reduced data are available in OI-FITS format³⁷ upon request.

Calibration Stars

The twenty-five nights of interferometric data span 2011 July 9-22 and 2013 September 12-30. For these nights of observation we use four calibration stars (37 Andromedae, γ Pegasi, γ

Trianguli, and 58 Ophiuchi) interspersed with observations of the target star ζ And. γ Peg, γ Tri, and 58 Oph are modeled as spherical, uniform disk stars³⁸ with their parameters included in Extended Data Table 2.

The calibrator 37 And is a recently-discovered binary system³⁹ with primary-to-secondary H -band flux ratio of 80 ± 20 . Ordinarily, binary stars make poor calibrators, but the 37 And system was observed enough times to determine its orbit precisely and salvage its use for calibrating our primary target ζ And. We detect the companion of 37 And in nineteen nights of data (see Extended Data Table 3) using a grid search for the companion. To constrain orbital parameters, we combined the visual orbit with the primary star's radial velocity curve obtained with archival spectra from the ELODIE high-resolution échelle spectrograph formerly on a 1.93-m telescope at Observatoire de Haute-Provence, France⁴⁰. Extended Data Figures 3 and 4 show the system orbit and radial velocity curve and Extended Data Table 4 contains the system orbital parameters. The orbital parameters are used in the MIRC calibration pipeline to account for the effect of the companion of 37 And.

SURFING imaging code

The image reconstruction code SURFING (SURFace imagING) was specially written for this project: to image surfaces of rotating stars. We create a global model of the star, including geometrical parameters (polar radius, oblateness, inclination, pole position angle, limb darkening coefficient, rotational period, epoch) as well as the surface temperature map. We cover the surface with tiles of equal area using the HEALPix methodology⁴¹, using 768 tiles to match the spatial resolution of CHARA. Each tile has an area of 0.025 mas^2 . We represent the shape of the stellar photosphere as a prolate spheroid to approximate a slightly partially-filling Roche potential. The deviation from spherical appears as gravity darkening and accounts for a

temperature difference of only ~ 60 K, which is much smaller than the temperature variations of the starspots.

We sampled the large range of geometrical models using an affine invariant ensemble Markov chain Monte Carlo approach⁴², with a nested loop to iteratively optimize the surface temperature map within each walker of the outer loop (this was needed as the 768 free parameters needed to characterize the temperature map would be intractable using a Markov chain approach). Extensive testing was carried out using blind simulated data to optimize the speed of convergence. In addition to minimizing the χ^2 statistic, we also incorporated priors on each parameter and could experiment with a variety of imaging regularizers, such as Total Variation (TV) or L2norm of wavelet coefficients.

In addition to testing the code on simulated data, we were also able to check results using soon-to-be-published data on the spotted star λ And²⁴, finding comparable results and confirming the inclination and position angle of the pole. We also checked that the imaging-derived orientation of another RS CVn (σ Gem, Roettenbacher et al. in preparation) matched the orbital plane of the close companion. The results of these tests and additional details about the implementation of our method will be described in a future paper (Monnier et al., in preparation).

ζ And Parameters from SURFING

Another test of the robustness of our fitting methodology is to determine the stellar orientation for independent data sets and compare the results. While the magnetic field structures will vary from year to year, the inclination of the pole and its position angle on the sky will not. Extended Figure 5 shows a χ^2 surface for three separate years: a 2008 pilot set of observations using the MIRC four-telescope system, the 2011 dataset, and the 2013 dataset. This figure shows two large regions of reduced χ^2 around inclination $i = 90^\circ$ and PA = -60° or

120°. These regions reflect the oblateness of the star and the basic orientation on the sky. The region near inclination $i = 70^\circ$, PA = 120° has the lowest χ^2 in all years, especially in 2013. This tells us the spots move from south-west toward north-east and not the other way around, and the consistent picture from year to year both shows the efficacy of the code and gives confidence that we are measuring true astrophysical signal and not over-fitting noise or systematic errors.

The results from these grid studies have been used to robustly estimate the geometrical parameters for ζ And, and these parameters are found in Table 1. The error bars associated with the parameters were determined by combining the results of data sets from 2011 and 2013, with the additional data from 2008. As the 2008 data were obtained with only four CHARA telescopes, they are not of high enough quality for imaging.

To convert H -band intensities from the reconstructed images into photospheric temperatures, we utilized Kurucz atmospheric models⁴³ for [Fe/H]=-0.25 and appropriate log g . Note that the overall temperature scale in our maps is uncertain (overall multiplicative scaling) due to lack of coeval photometry at H band; here we adopted mean H -band magnitude of $H = 1.64$ based on archival infrared photometry.

ζ And Imaging Tests

The previous section laid out our robust method for determining the geometrical parameters of ζ And by using three independent observing data from different years. The next issue is to determine the reliability of the surface temperature maps. We split the extensive CHARA/MIRC data from 2013 into two sets of seven nights each, alternating chronologically which night went to which set. Since spots take many days to cross the face of the star, each dataset should be viewing the same spots even though the timing was different. We present a comparison of the SURFING results in Extended Figure 6. Both partial datasets reproduce the

main features observed by the full dataset shown in the main text. This proves that the features seen in the maps are real and are not the result of an over-fitting to poor quality data or peculiarities of the nightly uv coverage.

The unprecedented phase coverage in the 2011 and (especially) the 2013 observing runs have allowed for textbook imaging fidelity tests for ζ And. We show the large-scale dark regions that cover ζ And are highly robust and statistically significant, likely deriving from magnetically-suppressed convection.

Code Availability

At present, we have opted not to make the SURFING code available because of a publication in preparation, which will detail the use and the applicability of the resource.

Methods References

31. Kiurkchieva, D. P. New analysis of II Peg 1977 light curve. *Astroph. Space Sci.*, **155**, 125-129 (1989).
32. Vogt, S. S. & Penrod, G. D. Doppler imaging of spotted stars – application to the RS Canum Venaticorum star HR 1099. *Pub. Astron. Soc. Pac.*, **95**, 565-576 (1983).
33. Harmon, R. O. & Crews, L. J. Imaging stellar surfaces via matrix light-curve inversion. *Astron. J.*, **120**, 3274-3294 (2000).
34. Monnier, J. D., et al. Imaging the surface of Altair. *Science*, **317**, 342-345 (2007).
35. Monnier, J. D., et al. Resolving Vega and the inclination controversy with CHARA/MIRC. *Astrophys. J. Let.*, **761**, L3 (2012).

36. Roettenbacher, R. M., et al. Detecting the companions and ellipsoidal variations of RS CVn primaries. I. σ Geminorum. *Astrophys. J.*, **807**, 23 (2015).
37. Pauls, T. A., Young, J. S., Cotton, W. D., & Monnier, J. D. A Data Exchange Standard for Optical (Visible/IR) Interferometry. *Pub. Astron. Soc. Pac.*, **117**, 1255-1262 (2005).
38. Bonneau, D., et al. SearchCal: a virtual observatory tool for searching calibrators in optical long baseline interferometry. I. The bright object case. *Astron. Astrophys.*, **456**, 789-789 (2006).
39. Baron, F. et al. CHARA/MIRC observations of two M supergiants in Perseus OB1: temperature, Bayesian modeling, and compressed sensing imaging. *Astrophys. J.*, **785**, 46 (2014).
40. Moultaq, J., Ilovaisky, S. A., Prugniel, P., and Soubiran, C. The ELODIE archive. *Pub. Astron. Soc. Pac.*, **116**, 693-698 (2004).
41. Górski, K. M., Hivon, E., Banday, A. J., Wandelt, B. D., Hansen, F. K., Reinecke, M., Bartelmann, M. HEALPix: A framework for high-resolution discretization and fast analysis of data distributed on the sphere. *Astrophys. J.*, **622**, 759-771 (2005).
42. Foreman-Mackey, D., Hogg, D. W., Lang, D., & Goodman, J. emcee: the MCMC hammer. *Pub. Astron. Sci. Pub.*, **125**, 306-312 (2013).
43. Kurucz, R. L. Model atmospheres for G, F, A, B, and O stars. *Astrophys. J. Sup. Ser.*, **40**, 1-340 (1979).

Extended Data Table 1 – Observations and calibrators of ζ And.

Extended Data Table 2 – Uniform disk sizes (*H*-band) of calibrators.

The uniform disk diameters were obtained with SearchCal³⁸.

Extended Data Table 3 – Binary separation and position angle measurements of 37 And.

Extended Data Table 4 – Orbital parameters of 37 And.

The orbital parameters were obtained by combining the ELODIE radial velocity curve with the CHARA/MIRC detections.

UT Date	Modified Julian Date (MJD)	Calibrators Used
2011 Jul 9	55751.536	37 And
2011 Jul 10	55752.531	γ Peg
2011 Jul 11	55753.480	37 And
2011 Jul 12	55754.469	γ Peg
2011 Jul 14	55756.478	γ Peg
2011 Jul 16	55758.505	58 Oph
2011 Jul 17	55759.481	γ Peg
2011 Jul 19	55761.475	37 And, γ Peg
2011 Jul 20	55762.517	γ Peg
2011 Jul 21	55763.478	γ Peg, γ Tri
2011 Jul 22	55764.480	γ Peg, γ Tri
2013 Sep 12	56547.449	37 And, γ Tri
2013 Sep 13	56548.426	37 And, γ Tri
2013 Sep 15	56550.392	37 And, γ Peg, γ Tri
2013 Sep 16	56551.365	37 And, γ Peg, γ Tri
2013 Sep 17	56552.345	37 And, γ Tri
2013 Sep 18	56553.359	37 And, γ Peg, γ Tri
2013 Sep 19	56554.407	37 And, γ Peg, γ Tri
2013 Sep 20	56555.365	37 And, γ Peg, γ Tri
2013 Sep 21	56556.403	37 And, γ Tri
2013 Sep 23	56558.403	37 And, γ Tri
2013 Sep 24	56559.343	37 And, γ Peg, γ Tri
2013 Sep 28	56563.367	37 And, γ Tri
2013 Sep 29	56564.357	37 And, γ Tri
2013 Sep 30	56565.334	37 And, γ Tri

Star Name (HD number)	θ_{UD} (mas)
γ Peg (HD 886)	0.41 ± 0.03
γ Tri (HD 14055)	0.51 ± 0.03
58 Oph (HD 160915)	0.68 ± 0.05

UT Date	Modified Julian Date (MJD)	Separation (mas)	Position Angle (°, E of N)	Error Ellipse Major Axis (mas)	Error Ellipse Minor Axis (mas)	Error Ellipse Position Angle (°)
2011 Jul 9	55751.492	11.46	217.0	0.13	0.11	300
2011 Jul 12	55754.499	9.09	230.6	0.10	0.08	270
2011 Jul 19	55761.465	6.38	295.4	0.06	0.05	330
2011 Nov 29	55894.159	63.57	143.9	1.82	0.16	340
2013 Sep 12	56547.470	82.28	152.6	0.58	0.15	330
2013 Sep 13	56548.399	82.51	152.7	0.02	0.10	30
2013 Sep 15	56550.340	82.47	152.8	0.81	0.26	350
2013 Sep 16	56551.344	82.73	152.9	1.23	0.27	340
2013 Sep 17	56552.329	82.63	152.9	0.48	0.17	330
2013 Sep 18	56553.250	82.88	153.0	0.95	0.21	340
2013 Sep 19	56554.292	83.06	153.1	0.72	0.27	350
2013 Sep 20	56555.301	83.02	153.2	0.79	0.14	330
2013 Sep 23	56558.416	83.08	153.4	1.01	0.22	340
2013 Sep 24	56559.239	83.29	153.5	0.58	0.23	340
2013 Sep 28	56563.303	83.62	153.7	1.08	0.21	340
2013 Sep 30	56565.276	83.65	153.8	0.83	0.20	340
2014 Aug 19	56888.422	14.45	98.2	0.32	0.18	280
2014 Aug 20	56889.446	15.58	100.8	0.24	0.17	10
2014 Sep 1	56901.412	22.82	116.9	0.11	0.07	300

Parameter	Value
Semimajor axis, a (mas)	46.66 ± 0.06
Eccentricity, e	0.8405 ± 0.0009
Inclination, i ($^\circ$)	52.5 ± 0.3
Argument of periastron, ω ($^\circ$)	168.9 ± 0.3
Ascending node, Ω ($^\circ$)	-17.6 ± 0.2
Orbital period, P_{orb} (days)	550.7 ± 0.2
Time of periastron passage, T_0 (MJD)	55765.45 ± 0.04
Velocity semi-amplitude, K_A (km/s)	11.1 ± 0.5
System velocity, γ (km/s)	5.33 ± 0.07

Extended Data Figure 1 – Visibility curve of UT 2013 September 15 observations of ζ And with CHARA/MIRC. The observed visibilities are plotted in black with 1σ error bars and the SURFING model visibilities are overlaid in red.

Extended Data Figure 2 – Closure phases of UT 2013 September 15 observations of ζ And with CHARA/MIRC. Each block represents a temporal block of observations with data plotted in black (with 1σ errors) and SURFING model in red.

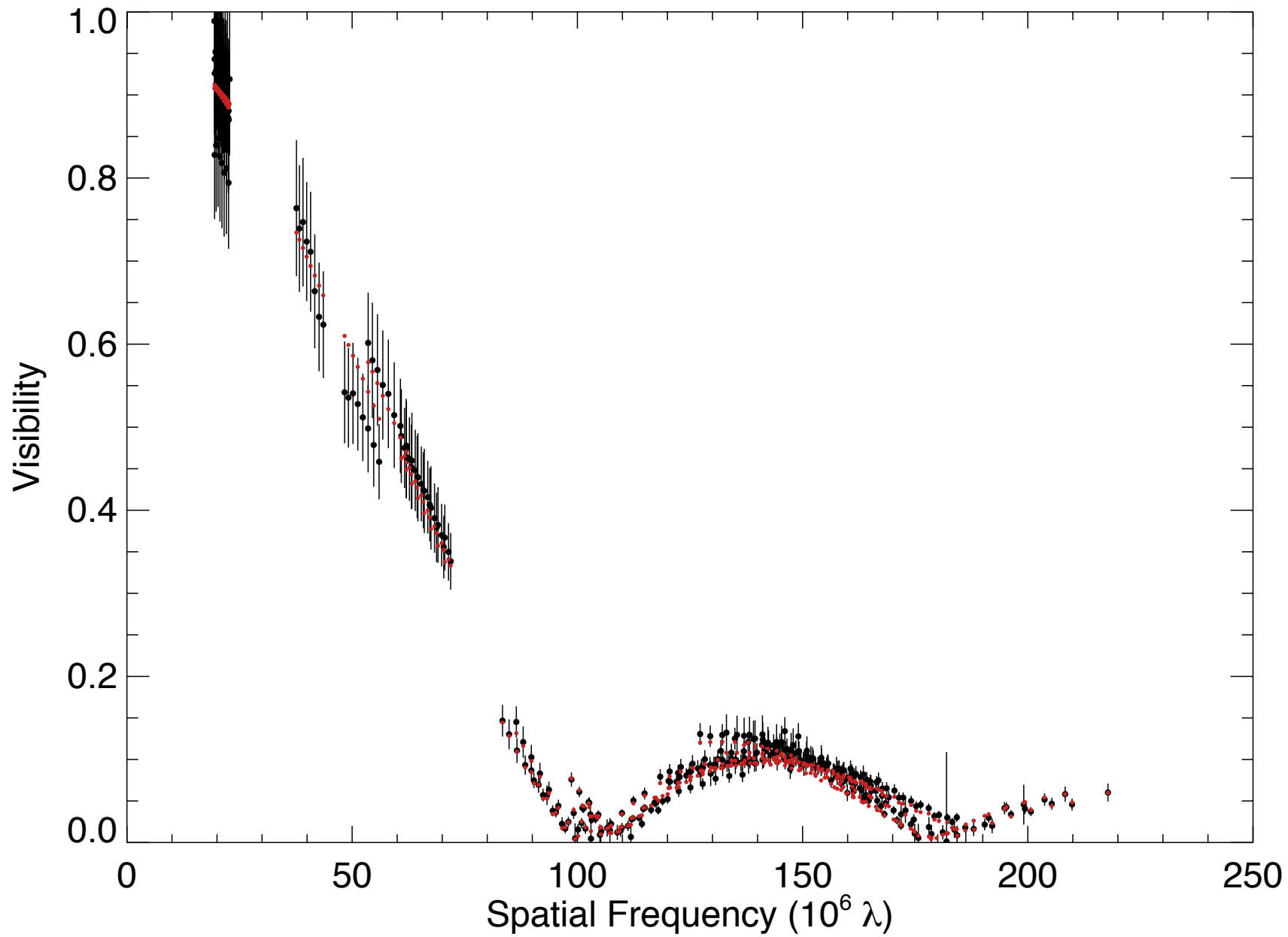
Extended Data Figure 3 – Orbit of 37 And. The gray plus signs represent measurements of the companion (1σ errors on detections are smaller than the symbols). The observed resolved disk of 37 And is plotted as the black dot at the origin. The thin solid black line is the best-fit orbit from combining the interferometric detections and the ELODIE radial velocities. Note: the axis units are milliarcseconds (mas) with north up and east to the left.

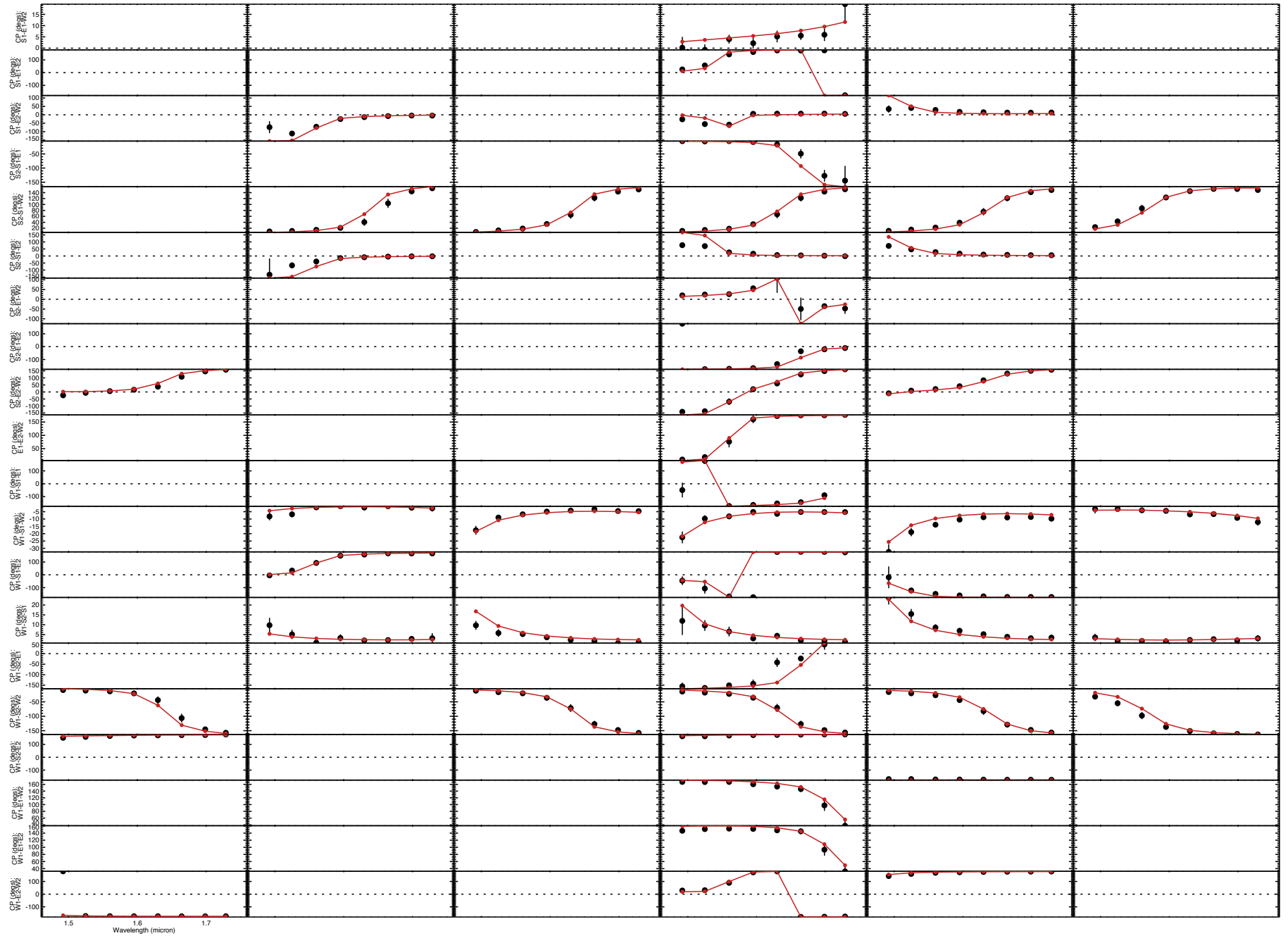
Extended Data Figure 4 – Radial velocity curve of the primary star of 37 And. The data points are based upon archival ELODIE spectra (with 1σ error bars). The orbital solution used the velocity measurements and the interferometric measurements simultaneously. The solid line is the best-fit orbit and the gray lines are fifty Monte Carlo realizations of the orbit.

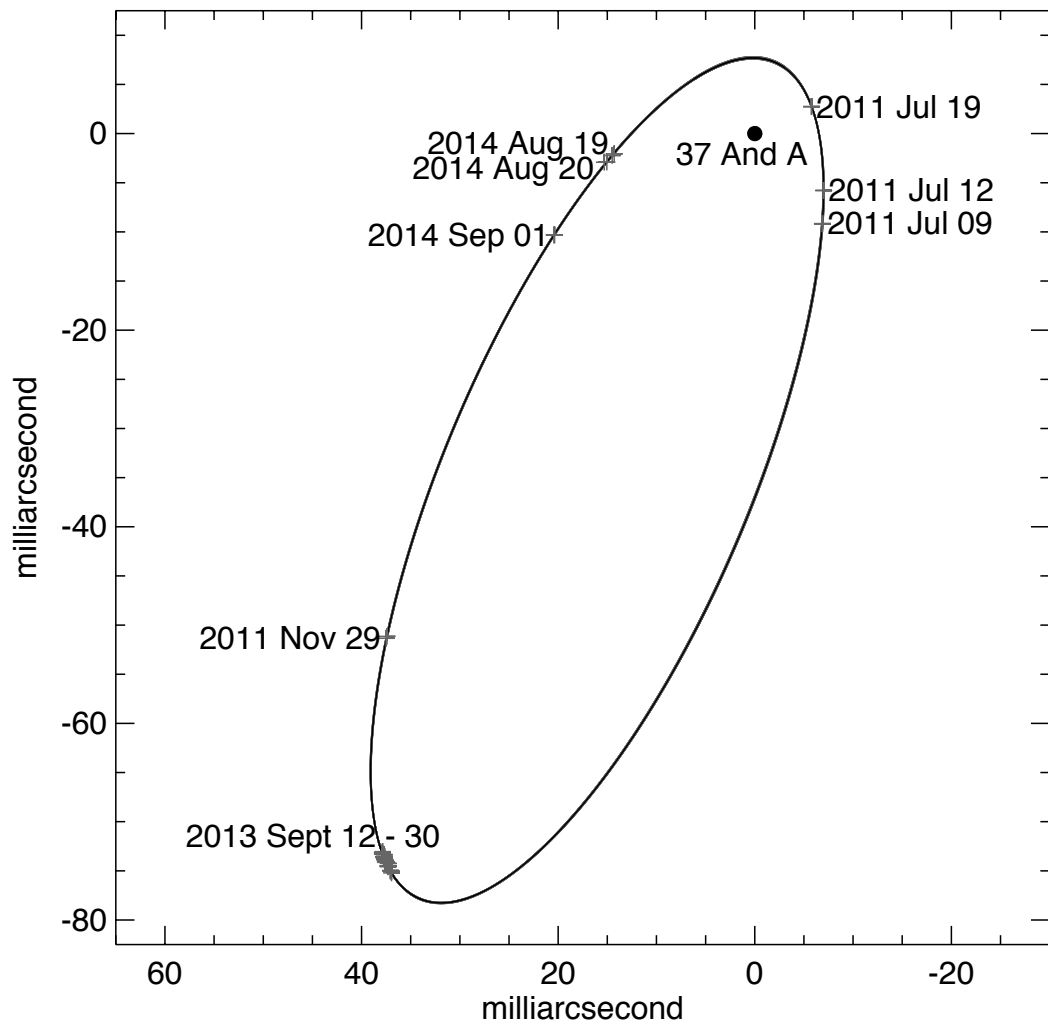
Extended Data Figure 5 – Reduced, normalized χ^2 surface plot of the SURFING model fit for position angle and inclination of ζ And. The peak is found at $PA = 126.0^\circ \pm 1.9$ and $i = 70.0^\circ \pm 2.8$. The epoch of each data set is located in the upper left of the panel.

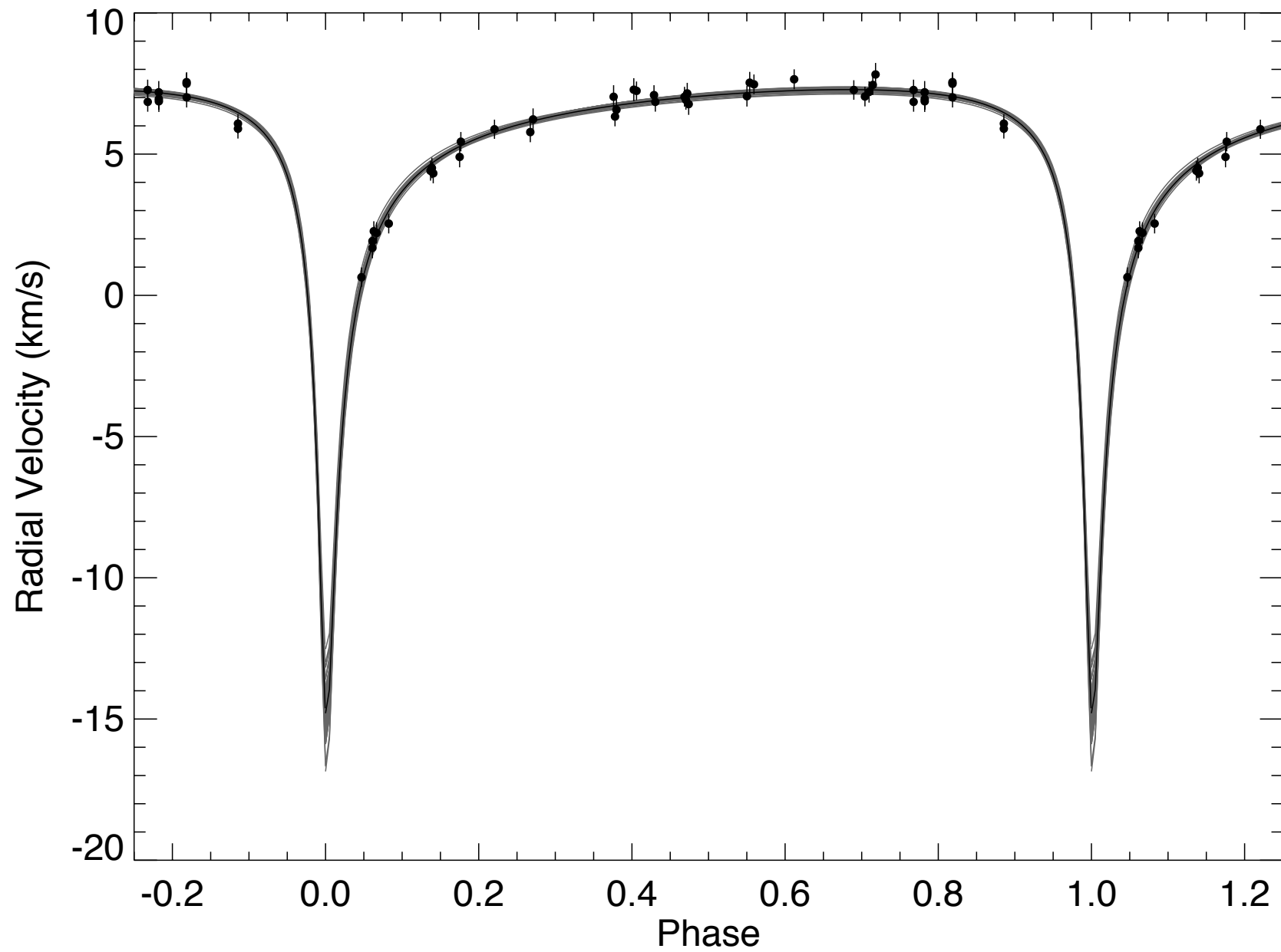
Extended Data Figure 6 – Comparison of the 2013 CHARA/MIRC data set divided into two sets of seven nights of data. These projections are plotted as the Aitoff projection in Figure

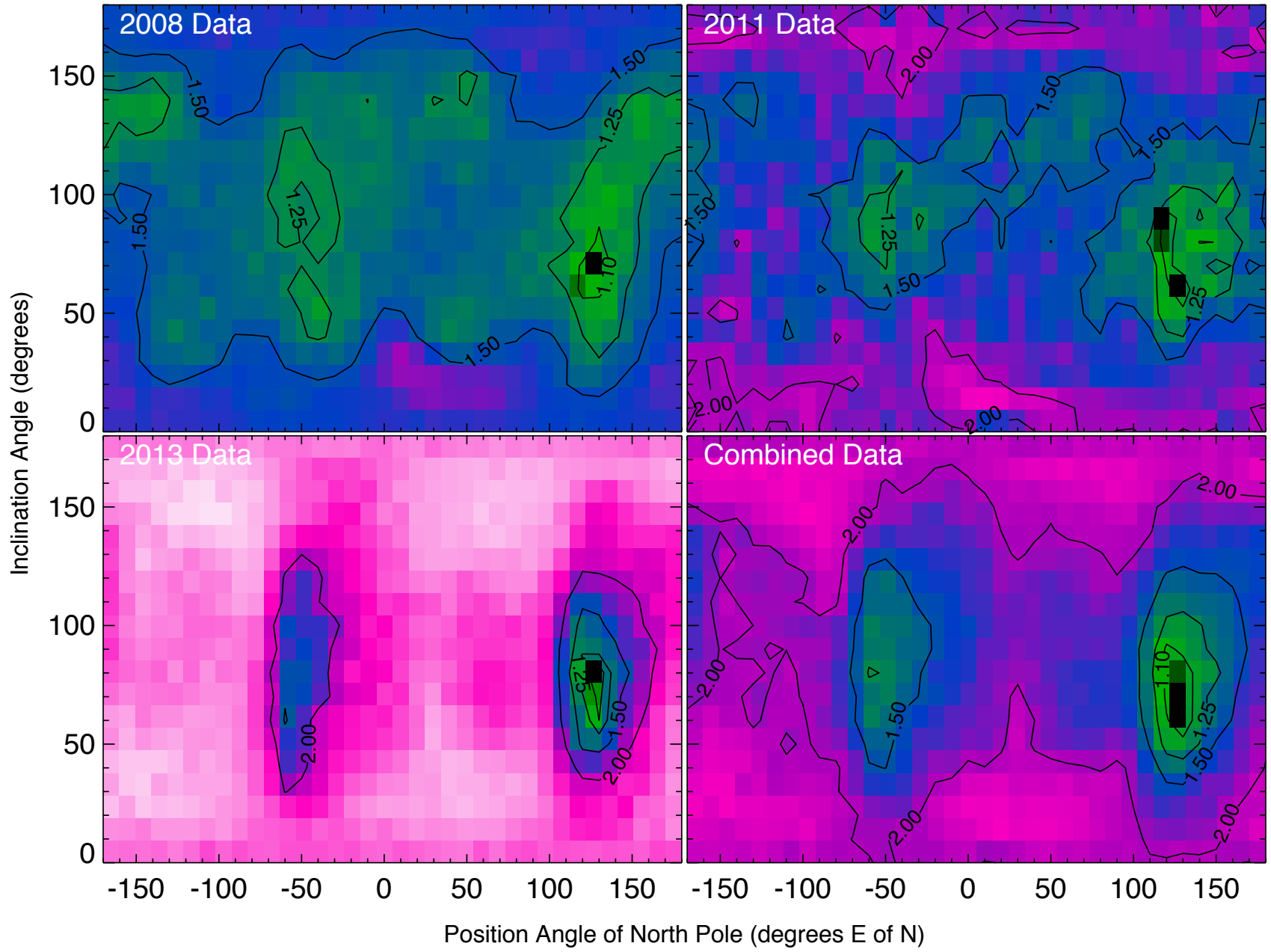
2.



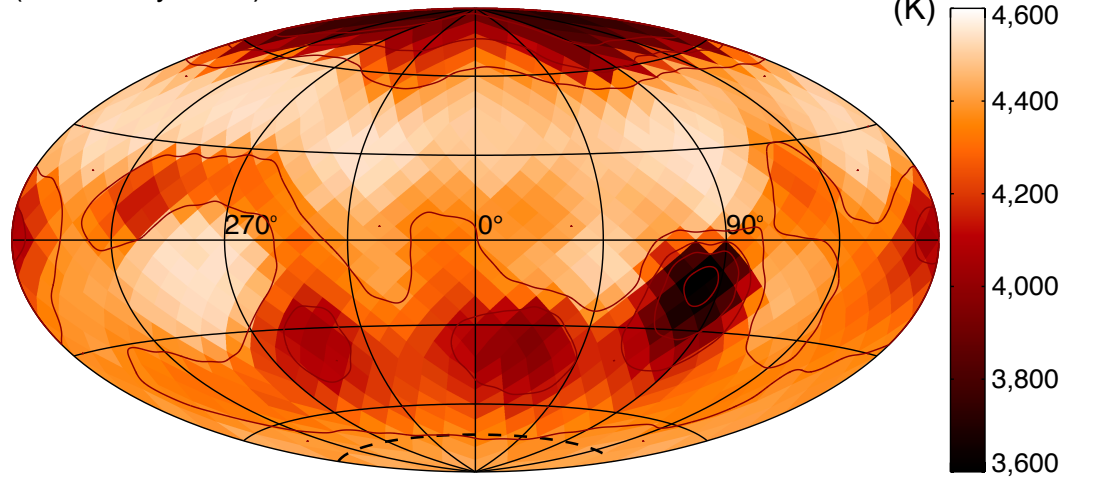








a 2013 Imaging of ζ And (Subset A)
(Aitoff Projection)



b 2013 Imaging of ζ And (Subset B)
(Aitoff Projection)

